



Research Article

Enhancement of hydroxyapatite dissolution through structure modification by Krypton ion irradiation

Hui Zhu^a, Dagang Guo^{a,*}, Hang Zang^{b,*}, Dorian A.H. Hanaor^c, Sen Yu^{a,d}, Franziska Schmidt^c, Kewei Xu^a

^a State Key Laboratory for Mechanical Behavior of Materials, School of Material Science and Engineering, Xi'an Jiaotong University, Xi'an, 710049, China

^b School of Nuclear Science and Technology, Xi'an Jiaotong University, Xi'an, 710049, China

^c Fachgebiet Keramische Werkstoffe/Chair of Advanced Ceramic Materials, Institut für Werkstoffwissenschaften und -Technologien, Technische Universität Berlin, Hardenbergstraße 40, 10623, Berlin, Germany

^d Shaanxi Key Laboratory of biomedical metal materials, Northwest Institute for Non-ferrous Metal Research, Xi'an, 710016, China



ARTICLE INFO

Article history:

Received 23 December 2018

Received in revised form 5 March 2019

Accepted 25 March 2019

Available online 5 September 2019

Keywords:

High energy heavy ion irradiation

Hydroxyapatite

HRTEM

Crystal defects

In vitro dissolution

Cell compatibility

ABSTRACT

Hydroxyapatite (HA) synthesized by a wet chemical route was subjected to heavy ion irradiation, using 4 MeV Krypton ion (Kr^{17+}) with ion fluence ranging from 1×10^{13} to 1×10^{15} ions/cm². Glancing incidence X-ray diffraction (GIXRD) results confirmed the phase purity of irradiated HA with a moderate contraction in lattice parameters, and further indicated the irradiation-induced structural disorder, evidenced by broadening of the diffraction peaks. High-resolution transmission electron microscopy (HRTEM) observations indicated that the applied Kr irradiation induced significant damage in the hydroxyapatite lattice. Specifically, cavities were observed with their diameter and density varying with the irradiation fluences, while a radiation-induced crystalline-to-amorphous transition with increasing ion dose was identified. Raman and X-ray photoelectron spectroscopy (XPS) analysis further indicated the presence of irradiation-induced defects. Ion release from pristine and irradiated materials following immersion in Tris (pH 7.4, 37 °C) buffer showed that dissolution *in vitro* was enhanced by irradiation, reaching a peak at 0.1 dpa. We examined the effects of irradiation on the early stages of the mouse osteoblast-like cells (MC3T3-E) response. A cell counting kit-8 assay (CCK-8 test) was carried out to investigate the cytotoxicity of samples, and viable cells can be observed on the irradiated materials.

© 2019 Published by Elsevier Ltd on behalf of The editorial office of Journal of Materials Science & Technology.

1. Introduction

Hydroxyapatite (HA), $\text{Ca}_{10}(\text{PO}_4)_6(\text{OH})_2$, exhibits natural biocompatibility and bioactivity as the dominant inorganic component of human bones. As proposed by Hench LL et al. [1], both bioactivity and biodegradability are the core requirements of the third-generation biomedical materials. However, the extremely slow degradation rate of HA cannot match the growth rate of newly formed bone *in vivo* [2]. It has been reported that a bone-bonding region at HA interfaces is achieved through extensive degradation/recrystallization events, which leads to better bone-ingrowth fixation [3,4]. That is, the degradation of calcium phosphate-based biomaterials has a strong impact on their osteoconductive prop-

erties [5,6]. Consequently, improving the degradation rate of HA has emerged as a key objective in recent biomaterial research. As reported, the *in vivo* degradation of Ca–P based biomaterials is mainly determined by its dissolution performance [7,8]. Various approaches have been taken towards enhancing the dissolution performance of HA, such as increasing the porosity [9,10], reducing the Ca/P ratio [11], decreasing the grain size or crystallinity [12], and ion substitution [13]. A.E. Porter et al. demonstrated through *in vitro/vivo* experiments that the dissolution of silicon (Si)-substituted HA started and propagated around structural defects [13–15]. Similarly, the dissolution of natural bone apatite such as human enamel is also driven by crystal defects, including abundant point defects, dislocations, stacking faults, and an amorphous grain boundary phase [16,17]. In general, it has been established that the amount and nature of defects in biological apatite govern its reactivity and solubility [16,18]. To date methods applied to enhance apatite dissolution, through defect engineering or otherwise, have

* Corresponding authors.

E-mail addresses: guodagang@mail.xjtu.edu.cn (D. Guo), zanghang@mail.xjtu.edu.cn (H. Zang).

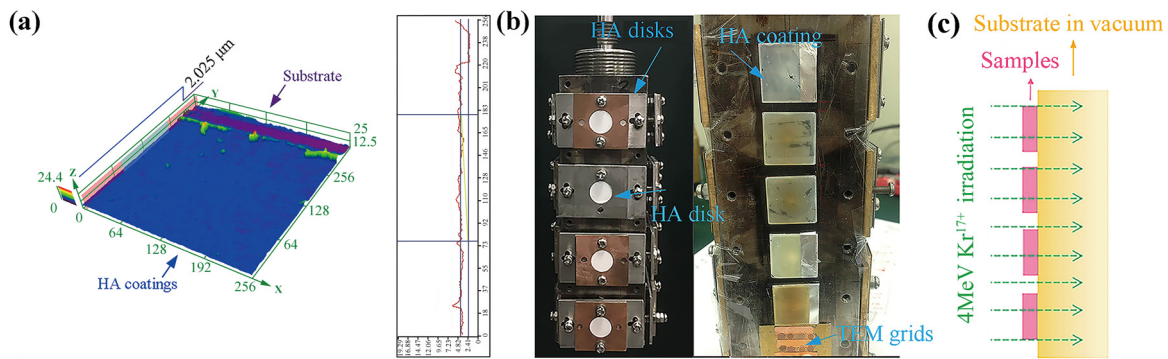


Fig. 1. (a) 3D surface morphology gradient map of a typical HA coating on a fused silica substrate. (b) Sample fixing setup for ion irradiation. (c) A diagram of irradiation process.

met with limited success, motivating the examination of further materials design approaches.

Heavy ion irradiation is a promising and effective technique to engineer the morphology and crystallinity of materials and thus modify their physicochemical properties. Through elastic and inelastic collisions with the nuclei and electrons of target atoms, energetic ions induce the displacement of atoms from their lattice positions resulting in defects and structural transformations [19]. B.D Begg et al. reported a “pyrochlore-to-fluorite” transformation in conjunction with amorphization triggered by irradiation [20]. This treatment was found to lead to a significant change in the material’s dissolution rate.

A few studies have examined the influence of ion irradiation on hydroxyapatite and its performance as a biomaterial. Reports have shown that ion irradiation of HA may increase its surface roughness, wettability, mechanical properties, cell adherence, and drug loading/release characteristics [21–26]. Improved levels of *in vitro* bioactivity of HA have been imparted while avoiding cytotoxicity by swift heavy ion irradiation with 100 MeV oxygen ions [26], and 125 MeV silicon ions [25]. These results indicate that high energy ion beam irradiation may serve as an effective method to enhance the biocompatibility and bioactivity of HA. Comparing with more commonly used techniques such as doping or substituting, ion irradiation has the advantage of altering the materials’ crystal structure without altering its stoichiometry. However, in general, the mechanisms through which ion irradiation affects the performance of bioceramics remain unclear and the dissolution performance of irradiated HA yet need to be examined. Gleaning further insights into the role of ion bombardment in biomaterials engineering necessitates direct examination of irradiation induced defects.

In the current study, we combine high-resolution transmission electron microscopy (HRTEM) with X-ray diffraction (XRD) to study the radiation-induced structural modification and the crystalline-to-amorphous transition of HA by 4 MeV Kr^{17+} ions. The effects of irradiation on the *in vitro* dissolution performance and *in vitro* cell response of HA are further examined. Through these studies, we provide a basic knowledge for a novel crystal structure engineering strategy to improve the degradation of HA.

2. Experimental

2.1. HA preparation

Stoichiometric HA [$\text{Ca}_{10}(\text{PO}_4)_6(\text{OH})_2$] was synthesized by a wet chemical method, previously described in greater detail [27]. Briefly, the pH of 0.5 M $\text{Ca}(\text{NO}_3)_2 \cdot 4\text{H}_2\text{O}$ and $(\text{NH}_4)_2\text{HPO}_4$ (SINOPHARM Group Co. Ltd, China) water solution were adjusted to 10.0 and 9.0 respectively by ammonia. The diammonium phos-

phate solution was then added to the solution of calcium nitrate slowly under stirring to yield a molar ratio of $\text{Ca}/\text{P} = 1.67$, and the solution was sealed following pH adjustment to 10.5. The reaction mixture was vigorously shaken at 50° for 48 h and then aged for 24 h. Precipitates were collected after washing. The paste was dried at 100°C under vacuum and ground manually. After sintering in a vacuum oven at 900° for 2 h, the obtained material was ground to yield a fine 200-mesh powder for TEM analysis.

2.2. Sample preparation

Samples were prepared in different forms prior to irradiation treatment. For TEM analysis, ultrasonically dispersed HA nanoparticles were deposited on copper TEM grids. For X-ray diffraction (XRD), Raman and XPS analysis, HA coatings were fabricated as follows: HA powder in ethanol was sonicated and stirred overnight to form a well-dispersed colloid. Fused silica substrates were pre-treated using a dilute HF solution and rinsed in DI water in turn. The substrates were cleaned in acetone, ethanol, and water ultrasonically, and then dried at 60°C . HA dispersions were deposited on the sheets followed by spinning at 8000 RPM for 40 s. After spinning, the thin coatings were dried for 10 min on a hot plate at 60°C . Thickness measurements, using Confocal Laser Scanning Microscopy (CLSM), confirmed a uniform thickness of approximately $2\ \mu\text{m}$ (Fig. 1(a)) from this process. For dissolution and cell studies, HA discs (2 mm height and 13 mm diameter) were uniaxially compacted from pure powders. All samples were fixed on a copper holder for perpendicular penetration by Kr^{17+} ions (Fig. 1(b)).

2.3. Ion irradiation

Irradiation experiments were carried out at the Institute of Modern Physics, Chinese Academy of Science (IMP CAS). Using the 320 kV multi-discipline research platform for highly charged ions materials, HA samples were irradiated by 4 MeV Kr^{17+} ions at room temperature, with fluences of 1×10^{13} , 2×10^{13} , 1×10^{14} , 2×10^{14} and 1×10^{15} ions/ cm^2 as shown in Fig. 1(c). The energy and fluences were selected to impart significant alteration of local structure with no residual radioactivity [28]. The local ionization and displacement densities per ion as a function of depth in HA under these irradiation conditions were determined from full cascade Monte Carlo calculations using the SRIM-2008 (Stopping and Range of Ions in Matter) code, with the output shown in Fig. 2. Default displacement energies of 25, 25, 28 and 10 eV for Ca, P, O and H, respectively [29,30]. The relative amount of damage arisen from nuclear collisions is given as displacements-per-atom (dpa): the average times each target atom has been displaced [31]. Fig. 2 reveals that Kr ion irradiation at 1.0×10^{15} ions/ cm^2 leads to irradiation damage of 0.5 dpa on the surface and a peak irradiation induced damage

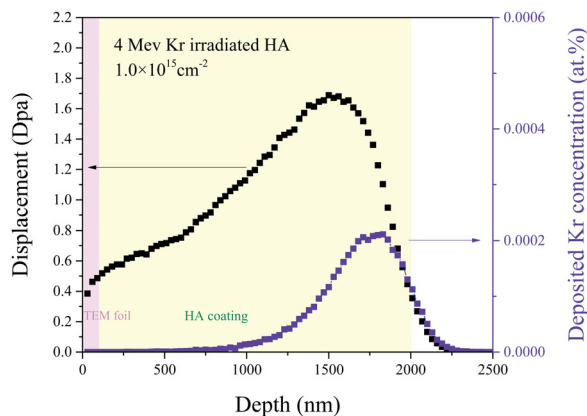


Fig. 2. SRIM simulation of the irradiation induced damage variations and Kr ion distribution with depth. Irradiation on the Cu foil and bulk Cu sample. Pink areas in the figures represent the 100-nm TEM foils and yellow areas represent the 2 μm HA coatings.

Table 1
Correspondence of dpa to ion fluences.

Sample label	Displacements-per-atom	Ion fluence
S0	0	0
S1	0.005 dpa	1×10^{13} ions/cm ²
S2	0.01 dpa	2×10^{13} ions/cm ²
S3	0.05 dpa	1×10^{14} ions/cm ²
S4	0.1 dpa	2×10^{14} ions/cm ²
S5	0.5 dpa	1×10^{15} ions/cm ²

of 1.7 dpa accompanied by a peak Kr deposition concentration of about 0.02%. As indicated by the pink regime on the left side of Fig. 2, irradiation penetration depth range is much larger than the TEM foil thickness (100 nm), and hence defects are expected to be uniformly introduced along with the specimen thickness. Krypton implantation effects can be neglected within this region. For the 2 μm coatings on silica substrates, the thickness of which is indicated by the yellow regime in Fig. 2, the damage varies with depth. However, this does not impede the analyses presented here. The final samples were denoted in Table 1.

2.4. Material characterization

Phase compositions of HA thin films before and after irradiation were determined by Glancing incidence X-ray diffraction (GIXRD) with CuK α radiation, using a scan speed of 2°/min and increment step of 0.077. On the basis of absorption calculations [32], a fixed incident angle of 1.5° was selected in order to examine the targeted penetration depth of 2 μm , corresponding to the thickness of the film. To image the irradiation induced defects, samples, before and after irradiation treatment, were examined in a JEM-2100 F HRTEM with an acceleration voltage of 200 kV. TEM imaging is known to induce lattice damage in HA materials. For this reason, imaging was conducted as briefly as possible to minimize electron irradiation influence. Energy-dispersive X-ray spectroscopy (EDS) and selected area electron diffraction (SAED) were performed on the irradiated samples as well. To examine bonding, Raman spectroscopy was employed over the range of shifts between 250 and 4,000 cm^{-1} in a backscattering geometry with 325 nm laser source on a confocal Horiba Jobin-Yvon HR800 spectrometer. The X-ray photoelectron spectroscopy (XPS) analyses were achieved by Al K α radiation for the excitation.

2.5. In vitro dissolution

The dissolution characteristics of pristine and irradiated materials were determined by a static immersion test. Each disc-shaped sample was coated on one side with impervious lacquer to yield a constantly exposed area. Then, discs were fixed by wax to the tip of a Teflon tube and immersed in tris (hydroxymethyl)-aminomethane (VWR. Co, US) solution with a pH of 7.4. The samples were sealed in PP Teflon containers at 37 °C for up to 14 days. The specimen area (mm^2) to solution volume ratio (mL) (SA/V) was 10:1 following the standard GB/T16886.14-2003 [33]. The solute concentrations of Ca²⁺ and PO₄³⁻ were measured from aliquots taken at various intervals by inductively-coupled-plasma (ICP) emission spectroscopy [IRIS Advantage (Thermo Scientific Ltd)]. The cumulative ion releases up to 14 days were calculated and plotted subsequently. For TEM characterization of dissolution effects, powders scraped from the irradiated HA coatings were immersed in deionized water.

2.6. In vitro cell culture studies

2.6.1. Cell culture

The biological performance of the as-prepared and irradiated HA discs was evaluated by using mouse osteoblast-like MC3T3 cells, obtained from cell banks of the Chinese Academy of Sciences (Shanghai, China). The culture medium was composed of Alpha Modified Eagle's medium (α -MEM, Hyclone, USA), 10% (v/v) fetal bovine serum (FBS, Zhejiang Tianhang Biotechnology Co., Ltd, China) and 1% penicillin-streptomycin (Sigma-Aldrich, USA).

2.6.2. Cell attachment and proliferation assay

All discs were sterilized by gamma rays (Co-60) of 25 kGy for 24 h. Approximately 80 mL of cell suspension (50000 cells/cm² mL⁻¹ for cell attachment and 25000 cells/cm² mL⁻¹ for cell proliferation, respectively) was poured on top of the discs gently. After 1 h at 37 °, the remaining medium was carefully added to the wells to cover the surface (1.0 mL). The medium was replaced every second day.

Cell attachment and morphology was observed after incubation for 24 h by scanning electron microscopy (SEM, FEI Quanta 400, Netherlands). Samples were washed twice with PBS solution and then fixed for 30 min in 0.1 M sodium-phosphate-buffered solution with 2.5% glutaraldehyde (Sinopharm, Shanghai, China). After washing twice with PBS solution, samples were dehydrated in ethanol with ascending concentrations (30, 50, 70, 90, 95, 100% (v/v)) for 10 min each, followed by immersion in pure hexamethyldisilazane for 10 min. Then they were dried in a desiccator overnight. The dried specimens were coated with gold for SEM observation.

Cell proliferation was evaluated after seeding cells followed by incubation for 1, 3, and 7 days following a cell counting kit-8 (CCK-8, Dojindo, Japan) assay. Briefly, the sample discs were first washed with PBS solution gently and then were carefully removed to a new 24-well plate. Afterward, each well with sample was flooded with 360 μL cell culture medium and 36 μL CCK-8 solution. After incubation at 37 °C for 3 h, 100 μL solution from each well of the 24-well plate was transferred to another 96-well cell culture plate quickly. The optical density (OD) was measured by a spectrophotometric microplate reader (GENios, Germany) with 450 nm wavelength. The OD values at days 3 and 7 were normalized to those at day 1.

2.6.3. Statistical analysis

One-way Anova was adopted for statistical analysis. Quintuple samples were used in each experiment to obtain the standard

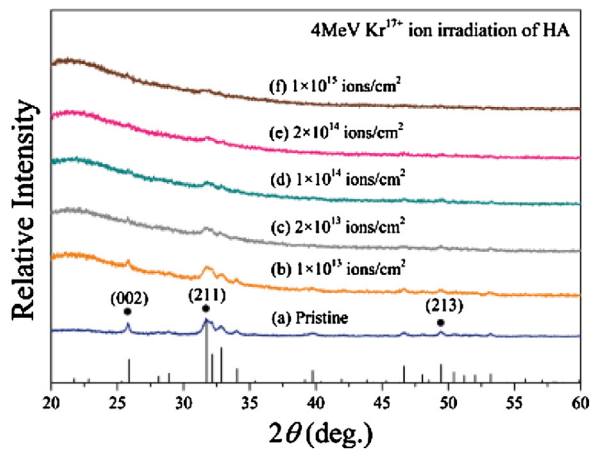


Fig. 3. GIXRD spectra of the irradiated and unirradiated HA coatings. Ion fluence: (a) 1×10^{13} to (f) 1×10^{15} ions/cm².

deviation. Statistically significant differences were considered at $p < 0.05$.

3. Results

3.1. XRD study

GIXRD was applied to analyze the crystalline structure in thin films samples on fused silica substrates. The depth of damage in irradiated HA was estimated to be 2.5 μm by SRIM (Fig. 2), meaning that the entire volume of the supported film experienced irradiation induced structural modification. Fig. 3 shows the diffraction peaks for HA coatings irradiated with 4 MeV Kr for various ion fluences. Compared with the JCPDS standard cards (#72-1243) of pure HA phase, no other phases were detected in irradiated materials. Notably, with increasing ion fluence, the intensities of (002) (211) and (213) diffraction peaks decreased and their widths increased, indicating lattice distortion. Furthermore, slight shifts of peaks to lower 2θ angles were observed. No impurity phases appeared after irradiation.

3.2. Formation of nanocavities during irradiation

To investigate local structure alteration, HA nanoparticles deposited on TEM copper grids were irradiated directly. Incident Kr ions passed through the grids completely. Fig. 4(a) shows the HRTEM images of HA nanoparticles before and after irradiation. Unirradiated particles exhibited grains without any vacancies or defects. Irradiation-induced cavities formed and developed with increasing dose. For S1 and S2 with low irradiation doses, significant cavities (mean diameter 5.6 nm to 6.7 nm) formed (marked by arrows). For an irradiation fluence of 1×10^{14} ions/cm² (S3), the original cavity diameter increased further to 8.2 nm approximately. Additionally, the second class of smaller cavities (approximately 2.4 nm) was also observed, particularly between the surface and the main layer. Continued Kr ion irradiation led to a doubling of the diameter of both the larger (14.1 nm) and smaller (6.9 nm) cavities, reaching a peak at a fluence of 2×10^{14} ions/cm² (S4). However, in specimens irradiated further to 1×10^{15} ions/cm² (S5), the mean diameters of the cavities were found to be significantly smaller. The evolution of cavity size with Kr fluence is shown in Fig. 4(b). Interestingly, the surface density of cavities exhibited a similar trend, showing a maximum in S5. Following the highest ion fluence of 1×10^{15} ions/cm², small cavities were found to be primarily located in close proximity to free surfaces, as such free surfaces may serve as a sink for point defects [34]. The EDS that was taken from S3 in

Fig. 4(d) shows no Kr peaks and a weakened oxygen peak compared to the unirradiated HA atomic arrangement of $\text{Ca}_{10}(\text{PO}_4)_6(\text{OH})_2$ (Fig. 4(c)).

3.3. Transmission electron microscopy analysis of ion irradiation induced “crystal-amorphous” transition

Bright field images of HA nanoparticles following irradiation at increasing fluences are shown in Fig. 5. The TEM photographs of Kr-irradiated HA nanoparticles indicated that Kr ion irradiation resulted in significant nanostructure modification. Fig. 5(a) corresponds to a typical TEM image of pristine material (unirradiated) showing a pure single crystal without evidence of defects, as evident from the undistorted lattice fringes. Small mottled contrast appears in S1 following an irradiation dose of 1×10^{13} ions/cm², as shown in Fig. 5(b). Some lattice fringes are discontinuous and they often manifest as noticeable edge dislocations, which are marked in Fig. 5(b) and its inverse fast Fourier transform (IFFT) in Fig. 5(c). The lattice spacing from Fig. 5(c) is found to be 0.281 nm, which closely matches the d-spacing of (211) planes of the HA lattice. Most regions are dominated by regular lattice stacking sequences, which reflects small disordering embedded in an otherwise undistorted crystal. Results indicate that at this irradiation dosage the apatite structure is largely intact, in agreement with XRD data. Following a dose of 2×10^{13} ions/cm² in S2, lattice stacking was still present in most regions; besides, greater distortion and twisting of the lattice fringes were evident. Planar defects such as grain boundaries constituted the dominant features (Fig. 5(d)). Additionally, in S2 shown in Fig. 5(e), amorphous bands were observed interrupting the crystal, which could originate from screw dislocations and be coordinated in a single parallel network [35]. After 1×10^{14} ions/cm² in S3, the degree of crystallinity continued to decrease, and the mottled regions formed a continuous amorphous network (Fig. 5(f)). The original crystal is broken into isolated tiny crystallites as shown in the Fast Fourier Transformation (FFT) patterns on the left side of Fig. 5(f), and the lattice fringes were disordered around the amorphous regions. Fig. 5(g) indicates that amorphization proceeds inwards under continued irradiation to 2×10^{14} ions/cm² in S4. A few crystalline islands were found, embedded in the amorphous matrix. FFT patterns from the inset of Fig. 5(g) shows that amorphization is indeed not complete. Finally, when the fluence exceeded 1×10^{15} ions/cm² or 0.5 dpa, the lattice image indicates a nearly fully amorphous state as shown in Fig. 5(h). Only mottled contrasts are observed without any lattice stacking sequences. Furthermore, the SAED patterns displayed in Fig. 5(i) confirmed the “crystal-to-amorphous” transformation triggered by irradiation as well. Overall, TEM images indicate a clear progressive increase in damage in HA nanoparticles by Kr irradiation: pristine samples exhibit regular structures, while with increasing ion irradiation the level of damage gradually increases until complete amorphization.

3.4. Raman spectroscopy

Raman spectra for apatite have been extensively studied. According to those studies, Raman active vibrations can be attributed to the following phonon modes: $\sim 962 \text{ cm}^{-1}$ to the ν_1 symmetric stretching vibration of phosphate anions (the most intense mode in the apatite spectrum), ~ 430 and $\sim 453 \text{ cm}^{-1}$ to the ν_2 symmetric out-of-plane bending modes, $\sim 1,052$ and $\sim 1,081 \text{ cm}^{-1}$ to the ν_3 antisymmetric stretching modes, and ~ 591 and $\sim 608 \text{ cm}^{-1}$ to ν_4 anti-symmetric bending, and the bond stretching mode associated with the OH group is detected as a sharp peak at 3572 cm^{-1} [36]. Fig. 6(a) shows the overall HA Raman spectra before and after irradiation. Raman shifts for different spectral regions are presented in Fig. 6(b–e). Decreased peak intensities and broadened full widths at half maximum (FWHM) are evident

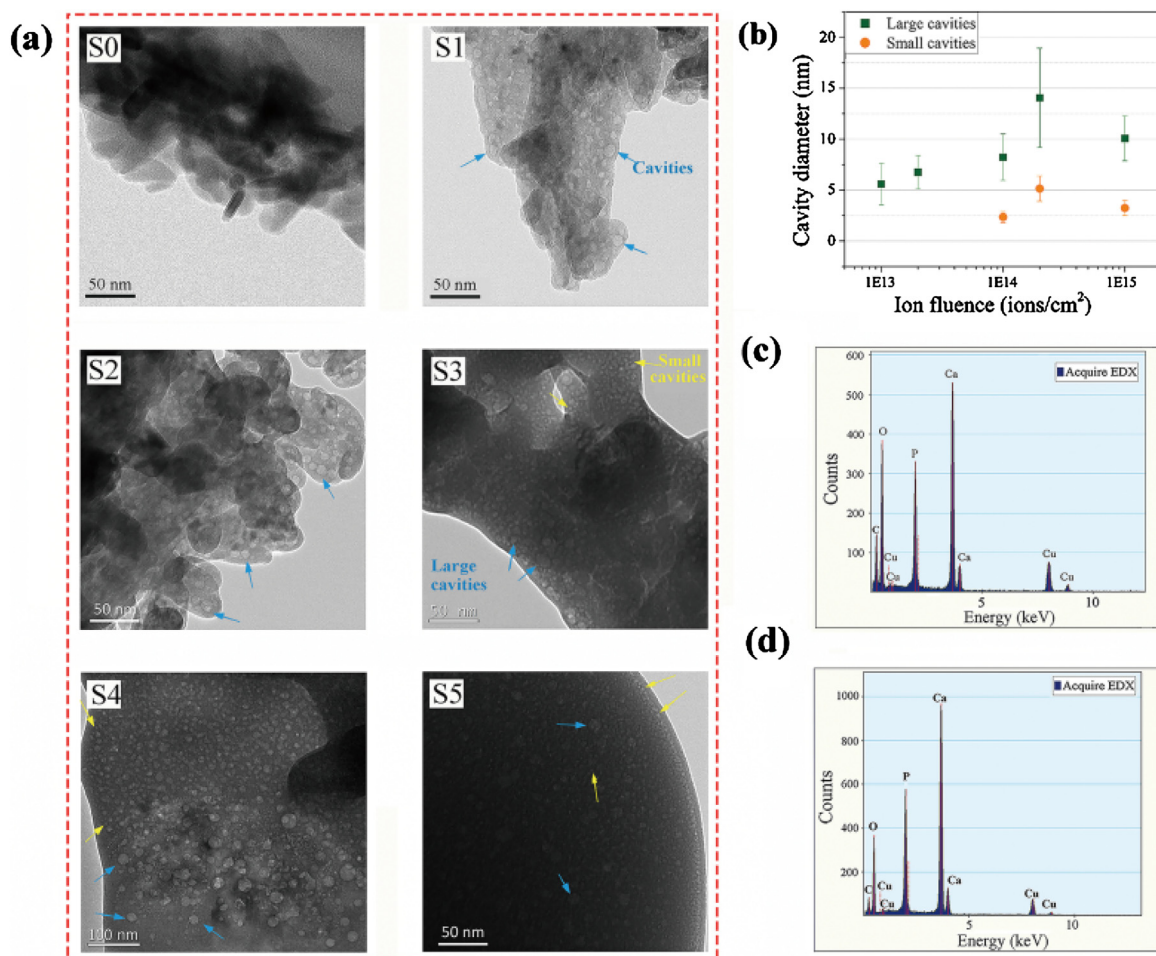


Fig. 4. (a) Cavities formation and evolution in the HA nanoparticles after irradiation with 4 MeV Kr^{17+} ions with increasing irradiation fluence at room temperature. (b) Cavity size variations upon the heavy ion fluence from TEM observations. (c) EDS spectrum taken from S0. (d) EDS spectrum taken from S3.

with increasing ion fluence. Notably, the ν_3 phonon peak and OH stretching almost disappear at 1×10^{14} ions/cm² and the previously separated and sharp modes disappear. Moreover, a red-shift could be observed with rising ion fluence as shown in Fig. 6(c). Those observations are all indicative of amorphization. The strongest ν_1 band (962 cm^{-1}) (inset in Fig. 6(c)) was further analyzed by deducing the evolution of its peak intensity, position and FWHM with deconvolution and least squares fitting of classical Poisson law [37,38]. Fig. 6f illustrates this peak's intensity evolving with ion fluence. Intensities decayed drastically from 2770.54 for the pristine material to 391.45 following a fluence of 1×10^{15} ions/cm². A Poisson's relation was employed here to fit the damage fraction in irradiated hydroxyapatite:

$$F_d = B[1 - \exp(-A\Phi t)] \quad (1)$$

where $A = \pi R^2$ presents the cross section for amorphization and B represents the maximal possible amorphization for hydroxyapatite [39,40]. According to the fitting results, the radius (R) can be calculated as 1.15 ± 0.27 , and the value of B can be obtained as 0.90 ± 0.02 . Based on this calculation, even the highest fluence cannot lead to a complete amorphization of hydroxyapatite, which disagrees with the above TEM results. However, it should be noted that it is very difficult to establish a straightforward correlation between damage in individual nanoparticle and the 'integrated' Raman spectrum due to the limited penetration depth and different Raman scattering cross-sections [31]. Fig. 6g-h show the evolution of peak positions and FWHMs of the ν_1 band with fluence. Those

trends are similar to the changes in peak position described above. In comparison with the non-irradiated sample, a maximum peak shift of 2.3 cm^{-1} was observed at the fluence of 1×10^{15} ions/cm². The shift could be attributed to the presence of residual stresses in the material induced by the growing quantity of cavities and defects in the irradiated samples [37].

It should be noted that a new broadband, centered around $\sim 945 \text{ cm}^{-1}$ can be observed after Kr^{17+} ion irradiation, becoming pronounced above the fluence of 2×10^{13} ions/cm² (Fig. 6c). It grows with the increment of ion fluence. This broadband (ν_{1b}) is formed from the ion irradiated amorphous cores [41]. The area ratio of ν_{1b} to the ν_1 symmetric stretching vibration of phosphate anions at 962 cm^{-1} was widely used for quantifying the amount of amorphization in different samples [38]. Following the same method, spectra were fractionally fitted by applying the Lorenz equation with the result reported in Fig. 6(e). As anticipated, the area ratio of ν_{1b} to ν_1 band increased gradually with ion fluence. For instance, it increased from 0.25 ± 0.04 to 6.06 ± 0.33 from 1×10^{13} to 1×10^{15} ions/cm², indicating a growing trend of amorphization.

3.5. XPS analysis

O 1s X-ray photoelectron spectroscopy of the samples and its fitting results before and after irradiation were also examined in Fig. 7 to support the inferences drawn from Raman spectroscopic studies. The first peak at 530.84 eV (I) is caused by O–P bonding and the second at 532.16 eV (II) is related to oxygen bonded to OH⁻ groups [42],

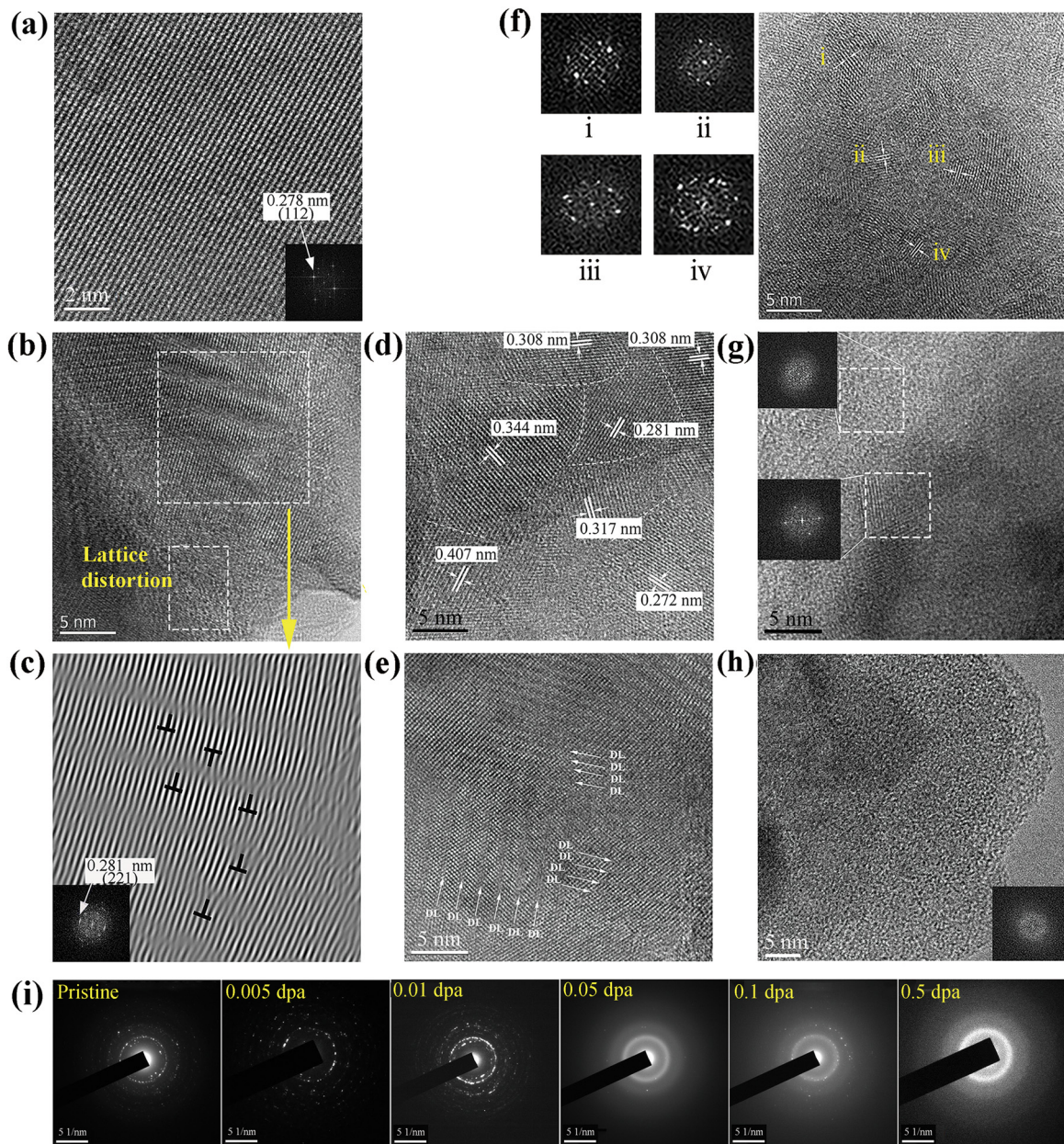


Fig. 5. Typical TEM images of the HA nanoparticles before and after Kr irradiation. (a) unirradiated, (b) 1×10^{13} ions/cm² (0.005 dpa) and (c) its inverse fast fourier transform, (d) and (e) 2×10^{13} ions/cm² (0.01 dpa), (f) 1×10^{14} ions/cm² (0.05 dpa), (g) 2×10^{14} ions/cm² (0.1 dpa), (h) 1×10^{15} ions/cm² (0.5 dpa), (i) SAED patterns of the sampels irradiated with various fluences.

or oxygen vacancies [43]. After ion irradiation, the binding energy of lattice oxygen (O–P) shifted slightly from 530.84 eV to 530.38 eV, and its area decreased by 29.79%. Whereas, the non-lattice oxygen (OH) binding energy shifted from 532.16 eV to 531.60 eV, with its area increasing by 173.71%.

3.6. Dissolution study

Fig. 8 shows the change in calcium and phosphate release in the Tris buffered solutions over 14 days of immersion. The curves in Fig. 8(a and b) show the impact of immersion time and Kr¹⁷⁺ ion irradiation fluence on Ca²⁺ and PO₄³⁻ release. All curves present an initial fast release of Ca²⁺ and PO₄³⁻ over the first 4 h immersion. The subsequent variations of Ca and P concentration were as follows: for pristine HA, Ca²⁺ concentration decreased after immersion for 4 h, and then fluctuated slightly until 3 days' immersion

before decreasing. For samples subjected to lower irradiation doses (S1 and S2), Ca concentrations decreased after 8 h soaking in Tris buffer and then remained stable from 1 to 3 days. Subsequently, a significant decrease occurred. However, for the samples under higher irradiation doses (S3–5), Ca concentrations remained constant from 8 to 24 h immersion, and then dropped intensely. All samples showed similar trends for their PO₄³⁻ release, which grows over the whole immersion in Tris buffer solution.

In addition, Fig. 8(a and b) shows that the ion release of irradiated HA was higher than pristine HA during their immersion in Tris buffer solution. Both Ca²⁺ and PO₄³⁻ concentration increased with the growing ion dose and then reached the maximum in S4 at 0.1 dpa (2×10^{14} ions/cm²) irradiation. The Ca²⁺ and PO₄³⁻ concentration of S4 increased by 51.30% and 133.57% respectively compared to the pristine one for 1 day's immersion (Fig. 8(c)). However, when the ion dose increased to 0.5 dpa, the ion release dropped.

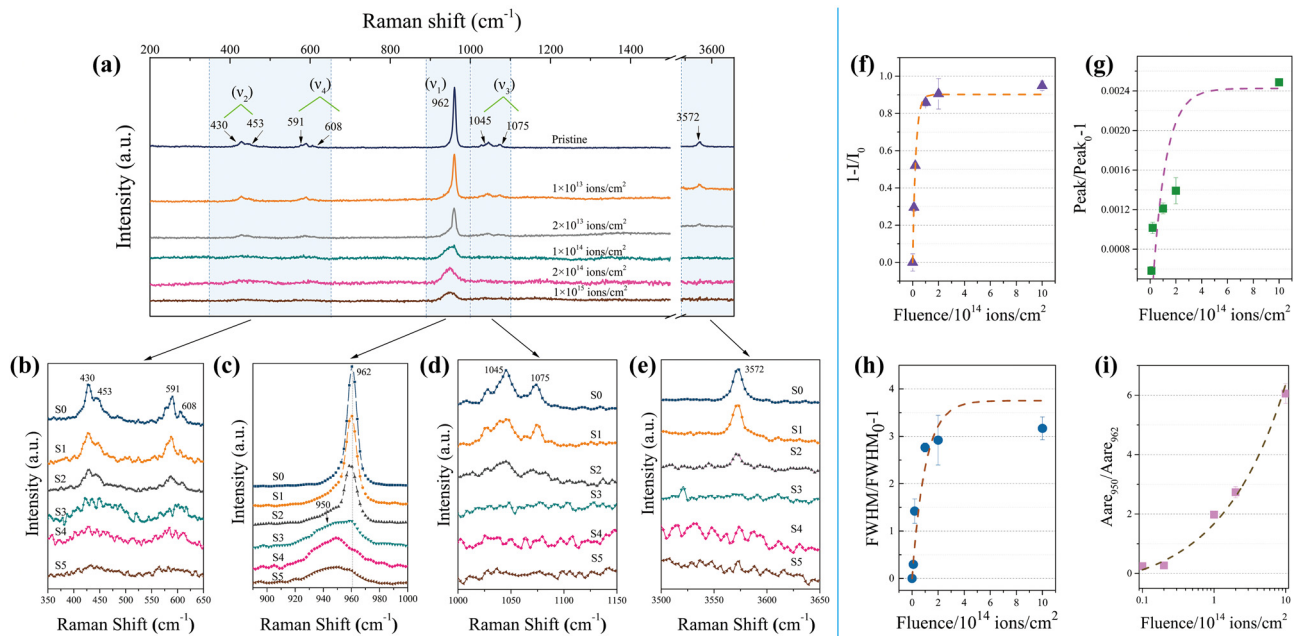


Fig. 6. Raman analysis: Spectra of samples irradiated at different doses are shown (a) over the full range of shifts, and in the shift ranges of (b) 350 to 650 cm^{-1} , (c) 890 to 1000 cm^{-1} , (d) 1000 to 1150 cm^{-1} , (e) 3500 to 3650 cm^{-1} . Decay of this band's intensity, change of its position, and the increase of its breadth as indicated by FWHMs are plotted as a function of ion fluence in (f), (g) and (h) respectively. (i) the area ratio of the radiation-induced broad ν_{1b} band (950 cm^{-1}) to the ν_1 band (962 cm^{-1}).

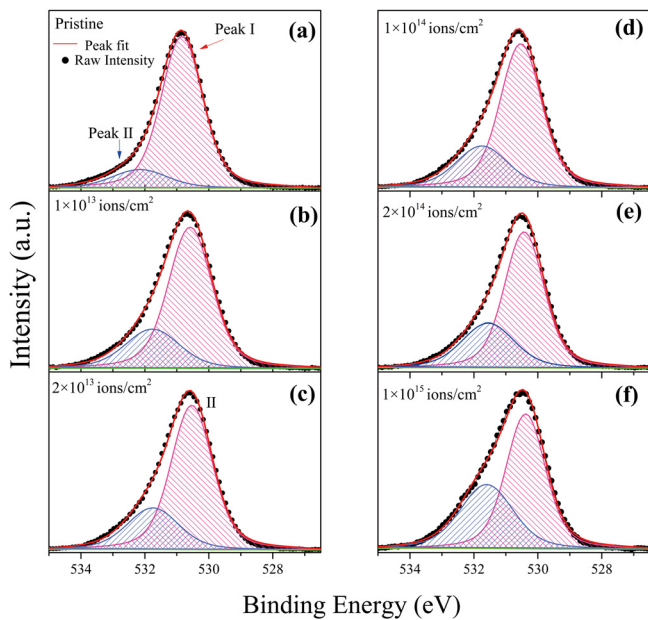


Fig. 7. XPS O 1s spectra for samples with increasing irradiation dose. (a) unirradiated, (b) 1×10^{13} ions/ cm^2 (0.005 dpa), (c) 2×10^{13} ions/ cm^2 (0.01 dpa), (d) 1×10^{14} ions/ cm^2 (0.05 dpa), (E) 2×10^{14} ions/ cm^2 (0.1 dpa), (f) 1×10^{15} ions/ cm^2 (0.5 dpa). In each subfigure, black markers show the data points, the solid red line shows the fitted profile and the two shaded areas show the deconvoluted contributions of the two binding energies.

To further understand the nanostructure variations of unirradiated and irradiated HA during dissolution, HRTEM observations were carried out for S0 and S4 respectively (Fig. 8(d)). After immersed in deionized water for 1 week, unirradiated HA presented a mottled grain surface which indicates the dissolution started from this region, while there was no sign of dissolution for the internal grain. In contrast, dissolution in irradiated HA initiated preferentially from defect structures inside grains, including grain boundaries and dislocations, with a corrugated disordered

appearance. After 2 weeks, the dissolution continued around those mottled regions on grain surfaces in unirradiated HA, showing a lamellar-like peeling dissolution mode. For the irradiated counterpart, dissolution developed around the grain distortions and grain surfaces as well, suggesting a deeper level of dissolution.

3.7. Cell culture study

The morphology of attached cells on sample surfaces was observed by SEM to assess the cytocompatibility of un- /irradiated samples at 24 h after cell seeding (Fig. 9(a–f)). MC3T3 cells attached and spread on all sample surfaces. After 24 h of culture, dense layers of cells with some filopodia extension were observed covering the entire unirradiated HA surface. For S1, Cells were connected to each other with the longest filopodia extensions compared to other groups. Simultaneously, some apatite-like grains can be detected on its surface. On the S2 surface, luxuriant growth and spread of cells can be seen with numerous filopodia, suggesting a good cell-materials attachment (Fig. 9(c)). Large numbers of spherical apatite particles were also observed as a result of mineralization. On the S3 and S4 irradiated surface, cells with unsatisfactory shapes could still interact with each other with shorter filopodia extension (Fig. 9(d and e)). A large number of apatite graduals formed beneath the cell layers. On the S5 surface (Fig. 9(f)), cells spread on the top of each other with a large density and intensive micro extensions.

Fig. 9(g and h) present the *in vitro* cytocompatibility results. Fig. 9(g) illustrates the numbers of attached cells on as prepared and irradiated HA surface with increasing irradiation fluence after 24 h' incubation. The OD values are widely used as a reliable measurement for the numbers of adherent cells on the specimen surface. In general, pristine HA had better cell attachment than irradiated HA (Fig. 9(g), $p < 0.05$ compared to unirradiated sample). S3 and S4 have the minimal number of adherent cells, indicating an unsatisfactory attachment. Fig. 9h presents the proliferation of MC3T3-E1 cells cultured on the as-prepared and irradiated HA surface as determined by CCK-8 assay. The irradiated sample with highest Kr ion fluence (0.5 dpa) exhibited a similar relative proliferation rate compared to the unirradiated counterpart at day 3 and day 7. However,

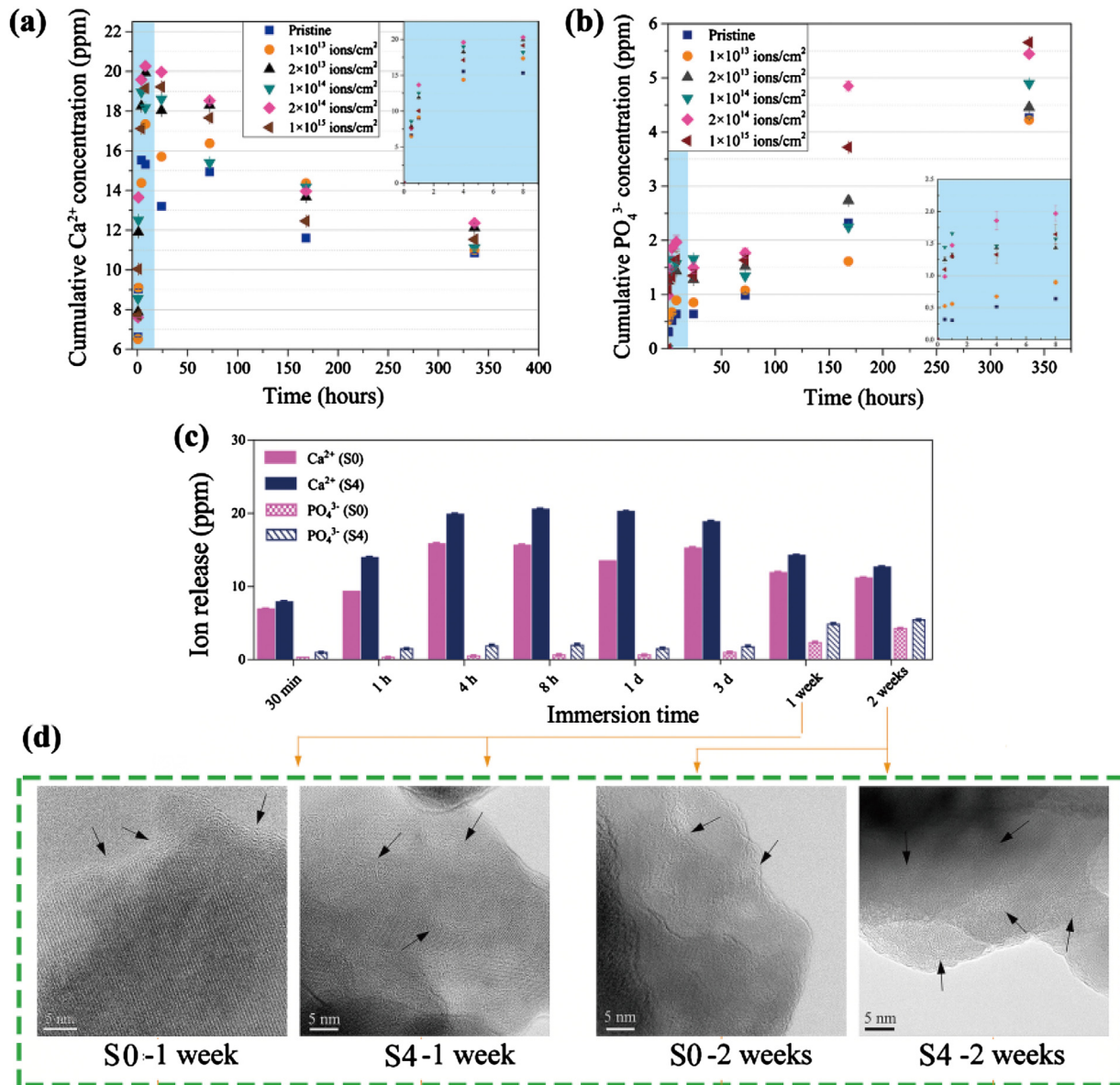


Fig. 8. (a) Calcium and (b) phosphate ions released in Tris-buffer solution from HA discs irradiated by 4 MeV Kr^{17+} ions with different fluences, with respect to immersion duration. Insets: enlarged view from 30 min to 8 h immersion. (c) Comparison of the ion release of pristine sample and 0.1 dpa irradiated samples. (d) HRTEM pictures of the pristine and 0.1 dpa irradiated samples after immersion for 1 and 2 weeks. Arrows indicate the dissolution starting points.

the other irradiated groups had lower proliferation rate of MC3T3-E1 cells than the unirradiated group, but no significant difference existed between them ($p < 0.05$).

4. Discussion

This current work for the first time explores the utility of dissolution enhancement by irradiation towards the design of functional HA biomaterials and explores the mechanisms of this enhancement to provide a theoretical and experimental basis for its implementation.

During the passage of heavy ions through the material, energy dissipation occurs through two mechanisms: elastic collisions with the nuclei of target atoms, and inelastic collisions with electrons, both of which generate structural damage. The atoms in the target migrate and hit the surrounding atoms leading to collision cascades [31,44]. The relationship of local structural damage and ion irradiation energy was obtained here by SRIM calculations, showing the

utility of the applied treatment for modifying crystalline hydroxyapatite in micron-scale depth regimes. As a result of collisions, vacancies are formed due to the displacement of atoms from their original lattice sites. As vacancies form and coalesce, voids can be formed [45]. If insoluble atoms (He, Xe, Kr, etc.) aggregate within irradiation-produced vacancies, small bubbles will be formed [46]. The cavities observed in this study (see Fig. 4) should be categorized as voids, rather than bubbles as the SRIM calculations shown in Fig. 2 indicate that following the highest irradiation level, negligible Kr implantation is expected within the geometry of the TEM foil (100 nm thickness). Further, EDS shows no evidence of Kr peaks (see Fig. 4 of 0.05 dpa irradiated HA). This suggests that the voids observed by HRTEM arise from the agglomeration of irradiation-induced vacancies, formed through atomic displacement cascades, rather than pressurized Kr bubbles. Supporting this, the deconvolution of XPS O1s spectra shows a decreasing ratio of lattice oxygen to non-lattice oxygen contributions (Fig. 7). This indicates the formation of irradiation induced oxygen vacancies, which may be the

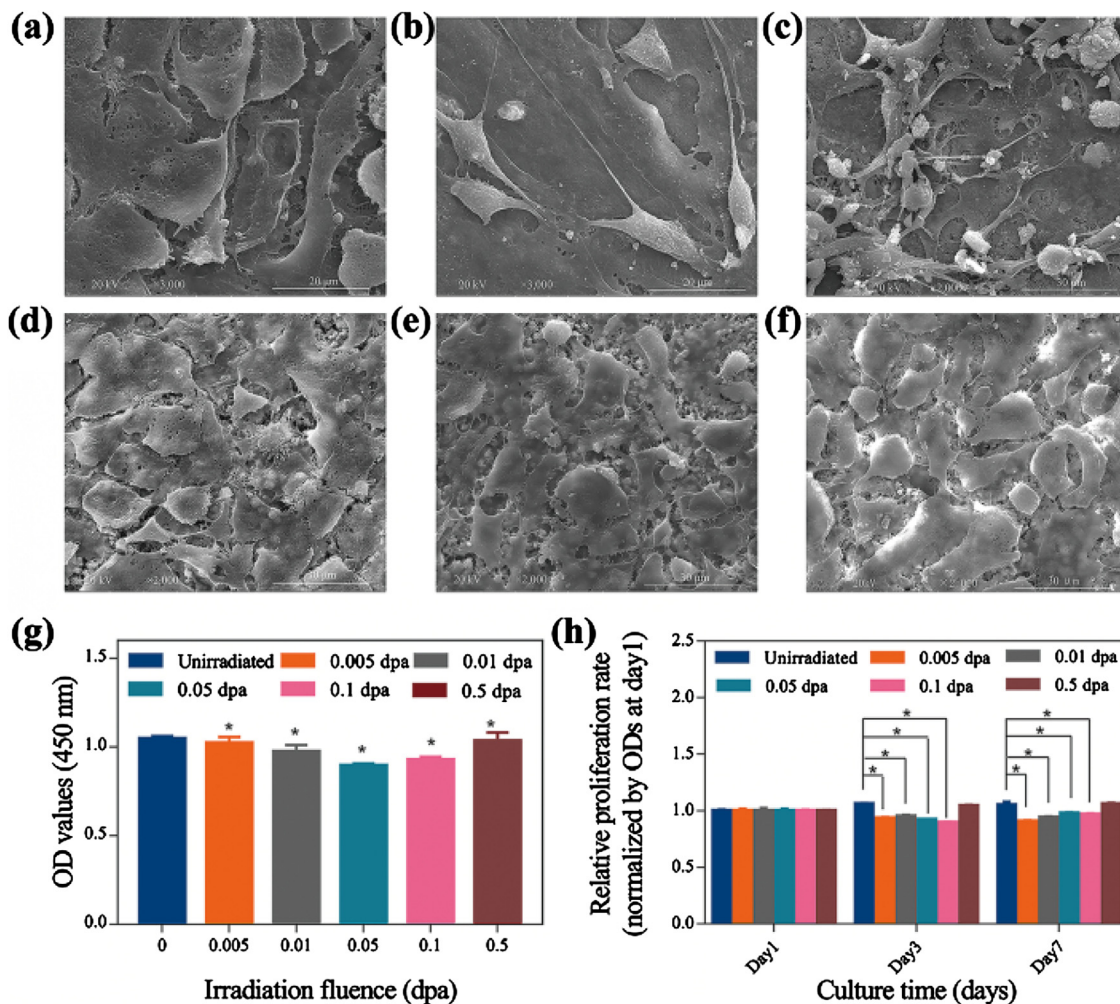


Fig. 9. Selected SEM images of cultured specimens ((a)–(f) 1×10^{13} to 1×10^{15} ions/cm²) at 24 h after MC3T3-E1 were seeded on their surfaces; (g) cell adhesion of MC3T3-E1 cells on the specimens at 24 h; (h) cell proliferation after cell seeding for 1, 3 and 7 days. The modified OD values at 3 and 7 days were normalized to those at 1 day. * denote $p < 0.05$.

origin of the observed voids [47]. Furthermore, the shift of the lattice component of O1s to lower binding energies confirms that defect formation is associated with electronic charge transfer, and the formation of oxygen vacancies [48]. The formation of oxygen vacancies is further supported by a notable decrease in the oxygen signal observed in EDS relative to Ca and P, although these data are not conducive to a quantitative interpretation.

The absence of significant void formation in pristine materials here suggests that beam damage did not play a role in present observations. In addition, the variation trend of mean void diameters with increasing ion fluences in Fig. 5 might be explained by the total swelling and the effect of surface energy [49].

Diffraction patterns from GIXRD (Fig. 2) clearly show an increasing amorphization with higher ion irradiation dose. The large baseline hump and the absence of significant peaks following the final dose indicate near complete disruption of long-range order in the HA crystal structure. No secondary phase formation is evident. Comparison with a related study involving 125 MeV Si⁹⁺ ion irradiated HA suggests 4 MeV Kr¹⁷⁺ irradiation yields a similar outcome [25]. The shift to lower 2θ angles implies lattice expansion accompanies the introduction of irradiation induced defects and structure disruption as observed elsewhere [32].

The observations of the present work lead to insights into the progression of structural defects in hydroxyapatite. It is postulated that oxygen vacancies are introduced by elastic collisions in

the lattice. The bonding energy of oxygen ions in the vicinity of vacancies is thus diminished and they are more readily vaporized, leading to further vacancies [50]. With increasing fluence, a network dislocation structure forms, which has been reported to act as an unsaturable sink for irradiation induced point defects [51]. The presence of unfaulted dislocations and network dislocations, as seen here, is an indicator of significant point defect mobility (Fig. 5(b)). As irradiation progresses, oxygen deficiency increases and the damage is enlarged [50].

The results of the present and previously published experiments indicate that introducing heavy ions can promote the formation and expansion of grain boundaries (Fig. 5(d and e)), which could provide the space for the movement of oxygen vacancies [52]. This is also considered as the beginning stage of polygonization. The relative disorder increases steadily with irradiation due to the accumulation of defect clusters and saturates after a crystal to amorphous transition. The threshold dose for complete amorphization of HA at room temperature under 4 MeV Kr¹⁷⁺ ion irradiation obtained in the present study was around 0.5 dpa, which is consistent with earlier research on apatite and other ceramic materials [53]. It should be noted that HRTEM observation has its limits considering the very localized and thin regions of the sample, nevertheless, diffraction results confirm the observed amorphous transition seen in these images. A summary of irradiation damage progression is presented in Table 2.

Table 2
A summary of irradiation damage progression of HA nanoparticles after irradiation.

Irradiation dose	HA crystal structures
0	Perfect lattice arrangement
0.005 dpa	Few dislocations and small mottled contrast
0.01 dpa	Grain boundaries and numerous dislocation lines. Considerable number of disorders
0.05 dpa	The original single crystal is broken into isolated crystallites with continuous amorphous phase.
0.1 dpa	Few crystalline regions embedded in the amorphous matrix. Lattice fringe are still visible
0.5 dpa	Completely amorphous HA particles.

Raman spectra have been widely used to verify structural variations in irradiated apatite [37,38,41,54], and similar results were obtained in this study. In general, irradiation induced defects and short-range disorder lead to a loss of intensity and broaden of bands [38] (Fig. 6). The blue shift of peak positions could further be due to the residual stress caused by irradiation [55]. Notably, the growing is the ratio of ν_{1b} to ν_1 at 964 cm^{-1} facilitates the quantitative measurement of lattice damage, which is difficult to achieve by XRD [37]. Nevertheless, a total amorphization was not detected even with the highest fluence from Raman results. A possible reason could be that Raman spectra are determined by local bonding structure rather than lattice spacing, this result may indicate the preservation of a consistent short-range order retained following irradiation induced disruption of the crystalline lattice.

The significant crystal structural variations in HA, arising from 4 MeV Kr^{17+} ion irradiation, were found to enhance the material's *in vitro* dissolution throughout the immersion process. Enhanced solubility is a natural consequence of the higher surface and bulk free energy induced by defects and amorphization. As can be seen in Fig. 8(a), maximum Ca^{2+} release took place in the first 24 h for all samples, before subsequently declining, which might be a result of the consumption of Ca^{2+} ions in the growth of apatite layers on sample surfaces [56]. Generally, it is seen here that the dissolution of HA, indicated by the release of Ca^{2+} and PO_4^{3-} was enhanced with an increasing density of crystal defects such as dislocations, grain boundaries and the expanding amorphous domains triggered by irradiation. This is inconsistent with studies into bone apatite, that have shown crystal defect sites are the initiation points for dissolution processes *in vivo/vitro* [15,57]. The ion concentration in bulk solution increased with irradiation damage in the range 0.005–0.1 dpa and decreased with further damage to 0.5 dpa. Interestingly, this follows the same trend of the diameter variation of voids produced by irradiation, shown in Fig. 4. This result demonstrates the significance of nanoscale porosity in enhancing dissolution and further suggests that ion vacancies may act as critical dissolution nuclei, as proposed in earlier reports [58].

To evaluate biocompatibility, in this study, cells were directly seeded on HA discs. Our results demonstrated that Kr^{17+} ion irradiation has a slight negative effect on the cell adhesion and cell proliferation on HA samples, however, cell attachment of S1, S2, S5 at 24 h and cell proliferation of S3, S4, S5 at 7 d are comparable with those of S1, which demonstrated that they have similar effects on cell activities. Considering the reported cell viability on HA synthesized by aqueous precipitation method, the cytocompatibility of the irradiated HA samples in this work was acceptable as well [59]. Contact angles were measured on all the disc samples for cell study with no significant differences detected (Fig. 10). Therefore, we postulate that the enhanced cell response to S5 is attributable to the different surface chemistry and topography of materials, as well as the decreasing dimensions of nanoparticles due to higher levels of amorphization [60]. While the somewhat impaired responses of S1–S4 understood in light of reports that elevated pH levels arising

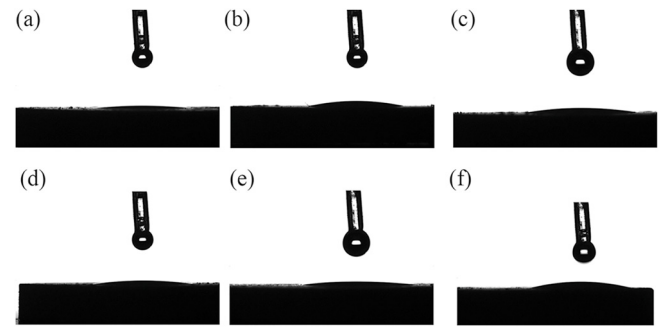


Fig. 10. Contact angle measurement of pristine and irradiated specimens with increasing irradiation fluences ((a)–(f) 1×10^{13} to 1×10^{15} ions/cm²).

from higher dissolution rates introduce a cytotoxic effect for cell proliferation and attachment [24].

Interestingly, the variation of attached cell numbers with irradiation fluence showed a similar trend to that of void diameters. A previous study has suggested that the presence of nanoscale voids in alumina exposes more cell-adhesive epitopes, promoting enhanced cell attachment [61]. Thus, it may be the case that the response of cellular adhesion proteins to the nano topology of irradiation modified HA is the reason for the observed cell attachment differences in our study.

It should be noted that in most cases, ion irradiation only influences surface material to a depth of several microns, without changing the bulk material's structure. Nevertheless, this strategy still has a broad significance towards biomedical applications, including coatings and composite systems, where interface modification has an important role to play. Overall results here demonstrate that heavy ion irradiation is applicable for tailoring both dissolution and biocompatibility, motivating further investigations into this complex relationship.

5. Conclusion

Through a combination of analytical approaches, heavy ion irradiation is shown to be an effective technique for crystal structure engineering in hydroxyapatite. Irradiation induces structural disorder, leading to the loss of crystallinity, formation of defects and nucleation of cavities with dose-dependent size and density. With sufficient heavy ion fluence, full amorphisation of hydroxyapatite can be achieved, accompanied by lattice oxygen deficiencies and nanoscale voids. The effects of ion irradiation on the atomic structure and microstructure of hydroxyapatite enhance the material's performance in terms of biodegradation as measured by *in-vitro* dissolution, with a maximal effect observed following an irradiation dose calculated to yield 0.1 displacement per atom. This treatment would not impart considerable cytotoxicity as measured by MC3T3 cell attachment and proliferation on samples surfaces. Results here shed further light on the mechanisms through which ion irradiation can facilitate the engineering of hard tissue repairing materials.

Acknowledgment

This work was supported by the Science Challenge Project [No: TZ2018004], National Natural Science Foundation of China [Nos. 51072159; 51273159], Science and technology program of Shaanxi Province [No: 2014K10-07], and Technology Foundation for Selected Overseas Chinese Scholar, Department of Human Resources and Social Security of Shaanxi Province [No: 2014-27]. The authors thank Jinyu Li and Tongmin Zhang (IMPCAS) for their help during the ion irradiation experiments.

References

- [1] L.L. Hench, J.M. Polak, *Science* 295 (2002) 1014–1017.
- [2] T. Thamaraiselvi, S. Rajeswari, *Carbon* 24 (2004) 172.
- [3] P. Ducheyne, J.M. Cuckler, *Clin. Orthop. Relat. Res.* 276 (1992) 102–114.
- [4] F.B. Bagambisa, U. Joos, W. Schilli, *J. Biomed. Mater. Res.* 27 (1993) 1047–1055.
- [5] R.Z. LeGeros, *Clin. Orthop. Relat. Res.* 395 (2002) 81–98.
- [6] M. Nagano, T. Nakamura, T. Kokubo, M. Tanahashi, M. Ogawa, *Biomaterials* 17 (1996) 1771–1777.
- [7] J. Lu, M. Descamps, J. Dejous, G. Koubi, P. Hardouin, J. Lemaitre, J.P. Proust, *J. Biomed. Mater. Res.* 63 (2002) 408–412.
- [8] H. Zhu, D. Guo, W. Qi, K. Xu, *Biomed. Mater.* 12 (2017), 015016.
- [9] S. Takagi, L.C. Chow, *J. Mater. Sci. Mater. Med.* 12 (2001) 135–139.
- [10] B.S. Chang, C.K. Lee, K.S. Hong, H.J. Youn, H.S. Ryu, S.S. Chung, K.W. Park, *Biomaterials* 21 (2000) 1291–1298.
- [11] H. Wang, L. Jong-Kook, M. Amr, J.J. Lannutti, *J. Biomed. Mater. Res. A* 67A (2003) 599–608.
- [12] W. Xue, L.X. Zheng, *J. Biomed. Mater. Res. A* 74A (2010) 553–561.
- [13] A.E. Porter, C.M. Botelho, M.A. Lopes, J.D. Santos, S.M. Best, W. Bonfield, *J. Biomed. Mater. Res. A* 69 (2004) 670–679.
- [14] A.E. Porter, S.M. Best, W. Bonfield, *J. Biomed. Mater. Res. A* 68 (2004) 133–141.
- [15] A.E. Porter, N. Patel, J.N. Skepper, S.M. Best, W. Bonfield, *Biomaterials* 24 (2003) 4609–4620.
- [16] G. Daculsi, B. Kerebel, *J. Biol. Buccale* 5 (1977) 203–218.
- [17] A. Krajewski, A. Ravaglioli, S. Wen, J. Feng, *J. Appl. Crystallogr.* 25 (1992) 465–470.
- [18] G. Daculsi, B. Kerebel, L.M. Kerebel, *Caries Res.* 13 (1979) 277–289.
- [19] S. Kuriakose, D. Avasthi, S. Mohapatra, *Beilstein J. Nanotechnol.* 6 (2015) 928.
- [20] B.D. Begg, N.J. Hess, W.J. Weber, R. Devanathan, J.P. Icenhower, S. Thevuthasan, B.P. McGrail, *J. Nucl. Mater.* 288 (2001) 208–216.
- [21] A.R. Ananda Sagari, P. Rahkila, M. Väisänen, R. Lehto, T. Sajavaara, S. Gorelick, M. Laitinen, M. Putkonen, S. Sangyuenyongpipat, J. Timonen, S. Cheng, H.J. Whitlow, *Nucl. Instrum. Methods Phys. Res. B* 266 (2008) 2515–2519.
- [22] K. Elayaraja, P. Rajesh, M.I. Ahymah Joshy, V. Sarath Chandra, R.V. Suganthi, J. Kennedy, P.K. Kulriya, I. Sulania, K. Asokan, D. Kanjilal, D.K. Avasthi, H.K. Varma, S. Narayana Kalkura, *Mater. Chem. Phys.* 134 (2012) 464–477.
- [23] C.M. Lopatin, T.L. Alford, V.B. Pizziconi, M. Kuan, T. Laursen, *Nucl. Instrum. Methods Phys. Res. B* 145 (1998) 522–531.
- [24] V. Nelea, H. Pelletier, D. Müller, N. Broll, P. Mille, C. Ristoscu, I.N. Mihailescu, *Appl. Surf. Sci.* 186 (2002) 483–489.
- [25] K. Elayaraja, M.I.A. Joshy, R.V. Suganthi, S.N. Kalkura, M. Palanichamy, M. Ashok, V.V. Sivakumar, P.K. Kulriya, I. Sulania, D. Kanjilal, K. Asokan, *Appl. Surf. Sci.* 257 (2011) 2134–2141.
- [26] R.V. Suganthi, S. Prakash Parthiban, K. Elayaraja, E.K. Girija, P. Kulariya, Y.S. Katharria, F. Singh, K. Asokan, D. Kanjilal, S. Narayana Kalkura, *J. Mater. Sci. Mater. Med.* 20 (2008) 271.
- [27] D. Guo, Y.Z. Hao, H.Y. Li, C.Q. Fang, L.J. Sun, H. Zhu, J. Wang, X.F. Huang, P.F. Ni, K.W. Xu, *J. Biomed. Mater. Res. Part B Appl. Biomater.* 101 (2013) 1275–1283.
- [28] G.S. Was, *J. Mater. Res.* 30 (2015) 1158–1182.
- [29] B.J.P. Ziegler J F, 2008 Program TRIM. <<http://www.srim.org>>.
- [30] L.M. Wang, R.C. Ewing, M. Cameron, W.J. Weber, In situ observation of radiation induced amorphization of crystals with apatite structure, *Spring Meeting Mater. Res. Soc.* (1993).
- [31] O. Lehtinen, T. Nikitin, A.V. Krashennnikov, L.T. Sun, F. Banhart, L. Khriachtchev, J. Keinonen, *New J. Phys.* 13 (2011) 19.
- [32] J.X. Xue, G.J. Zhang, L.P. Guo, H.B. Zhang, X.G. Wang, J. Zou, S.M. Peng, X.G. Long, *J. Eur. Ceram. Soc.* 34 (2013) 633–639.
- [33] C.N.S.M.C. AQSIQ GB/T16886.14-2003 Medical Biological Evaluation, Part 14: Degradation Product of Pottery and Porcelain Qualitative and Quantitative, Standards Press of China, 2003.
- [34] W. Gong, L. Wang, R. Ewing, *J. Appl. Phys.* 84 (1998) 4204–4208.
- [35] P. Houllé, J.C. Voegel, P. Schultz, P. Steuer, F.J. Cuisinier, *J. Dent. Res.* 76 (1997) 895–904.
- [36] P. Comodi, Y. Liu, M.L. Frezzotti, *Phys. Chem. Miner.* 28 (2001) 225–231.
- [37] S. Miro, J. Costantini, J. Bardeau, D. Chateigner, F. Studer, E. Balanzat, J. Raman Spectrosc. 42 (2011) 2036–2041.
- [38] M. Weikusat, U.A. Glasmacher, B. Schuster, C. Trautmann, R. Miletich, R. Neumann, *Phys. Chem. Miner.* 38 (2011) 293–303.
- [39] F. Villa, M. Grivet, M. Rebetez, C. Dubois, A. Chambaudet, N. Chevarier, G. Blondiaux, T. Sauvage, M. Toulemonde, *Nucl. Instrum. Methods Phys. Res. B* 168 (2000) 72–77.
- [40] M. Toulemonde, *Applied Radiation, Isotopes.* 46 (1995) 375–381.
- [41] J. Liu, U.A. Glasmacher, M. Lang, C. Trautmann, K.O. Voss, R. Neumann, G.A. Wagner, R. Miletich, *Appl. Phys. A* 91 (2008) 17–22.
- [42] M.A. Baker, S.L. Assis, O.Z. Higa, I. Costa, *Acta Biomater.* 5 (2009) 63–75.
- [43] R.S. Lubna, A. Bakhtyar, Z. Hao, W.G. Wang, Y.Q. Song, H.W. Zhang, S.I. Shah, J.Q. Xiao, *J. Phys. Condens. Matter* 21 (2009), 486004.
- [44] J.F. Ziegler, J.P. Biersack, M.D. Ziegler, SRIM : The Stopping and Range of Ions in Matter, SRIM, Chester (Md.), 2008.
- [45] J. Reyes-Gasga, R. Garcia-Garcia, E. Brès, *Physica B Condens. Matter* 404 (2009) 1867–1873.
- [46] M. Fell, S.M. Murphy, *J. Nucl. Mater.* 172 (1990) 1–12.
- [47] B. Bharti, S. Kumar, H.-N. Lee, R. Kumar, *Sci. Rep.* 6 (2016) 32355.
- [48] K.I. Maslakov, Y.A. Teterin, A.J. Popel, A.Y. Teterin, K.E. Ivanov, S.N. Kalmykov, V.G. Petrov, P.K. Petrov, I. Farnan, *Appl. Surf. Sci.* 448 (2018) 154–162.
- [49] S.T. Rosinski, M.L. Grossbeck, T.R. Allen, A.S. Kumar, Effects of Radiation on Materials: 20th International Symposium, ASTM International, 2001.
- [50] T. Lu, L. Lin, X. Zu, S. Zhu, L. Wang, *Nucl. Instrum. Methods Phys. Res. B* 218 (2004) 111–116.
- [51] S. Zinkle, S. Kojima, *Nucl. Instrum. Methods Phys. Res. B* 46 (1990) 165–170.
- [52] X. Yan, Y. Li, J. Zhao, Y. Li, G. Bai, S. Zhu, *Appl. Phys. Lett.* 108 (2016), 033108.
- [53] L. Wang, W. Weber, *Philos. Mag. A* 79 (1999) 237–253.
- [54] K. Elayaraja, P. Rajesh, M.A. Joshy, V.S. Chandra, R. Suganthi, J. Kennedy, P. Kulriya, I. Sulania, K. Asokan, D. Kanjilal, *Mater. Chem. Phys.* 134 (2012) 464–477.
- [55] I. De Wolf, *Semicond. Sci. Technol.* 11 (1996) 139.
- [56] Z. Mohammadi, A. Ziaei-Moayyed, A.S.-M. Mesgar, *Biomed. Mater.* 3 (2008), 015006.
- [57] J. Arends, W.L. Jongebloed, *Caries Res.* 11 (1977) 186–188.
- [58] S.V. Dorozhkin, *Prog. Cryst. Growth Charact. Mater.* 44 (2002) 45–61.
- [59] S.C. Cox, P. Jamshidi, L.M. Grover, K.K. Mallick, *J. Mater. Sci. Mater. Med.* 25 (2014) 37–46.
- [60] S. Samavedi, A.R. Whittington, A.S. Goldstein, *Acta Biomater.* 9 (2013) 8037–8045.
- [61] T.J. Webster, L.S. Schadler, R.W. Siegel, R. Bizios, *Tissue Eng.* 7 (2001) 291–301.